JACS
JOURNAL OF THE AMERICAN CHEMICAL SOCIETY

Article

pubs.acs.org/JACS

Application of Consistency Criteria To Calculate BET Areas of Micro- And Mesoporous Metal–Organic Frameworks

Diego A. Gómez-Gualdrón,[†,∥] Peyman Z. Moghadam,[†,∥] Joseph T. Hupp,[‡] Omar K. Farha,[‡,§] and Randall Q. Snurr*[,†]

[†]Department of Chemical and Biological Engineering and [‡]Department of Chemistry, Northwestern University, Evanston, Illinois 60208, United States

[§]Department of Chemistry, Faculty of Science, King Abdulaziz University, Jeddah 22254, Saudi Arabia

Supporting Information

ABSTRACT: Metal–organic frameworks (MOFs) can exhibit exceptionally high surface areas, which are experimentally estimated by applying the BET theory to measured nitrogen isotherms. The Brunauer, Emmett, and Teller (BET)-estimated nitrogen monolayer loading is thus converted to a "BET area," but the meaning of MOF BET areas remains under debate. Recent emphasis has been placed on the usage of four so-called "BET consistency criteria." Using these criteria and simulated nitrogen isotherms for perfect crystals, we calculated BET areas for graphene and 25 MOFs having different pore-size distributions. BET areas were compared with their corresponding geometrically calculated, nitrogen-accessible surface areas (NASAs). Analysis of simulation snapshots elucidated the contributions of "pore-filling" and "monolayer-formation" to the nitrogen adsorption loadings in different MOF pores, revealing the origin of inaccuracies in BET-calculated monolayer loadings, which largely explain discrepancies between BET areas and NASAs. We also find that even if all consistency criteria are satisfied, the BET calculation can significantly overestimate the true monolayer loading, especially in MOFs combining mesopores ($d \geq 20$ Å) and large micropores ($d = 10–20$ Å), due to the overlap of pore-filling and monolayer-formation regimes of these two kinds of pores. While it is not always possible to satisfy all consistency criteria, it is critical to minimize the deviation from these criteria during BET range selection to consistently compare BET areas of different MOFs and for comparing simulated and experimental BET areas of a given MOF. To accurately assess the quality of a MOF sample, it is best to compare experimental BET areas with simulated BET areas rather than with calculated NASAs.

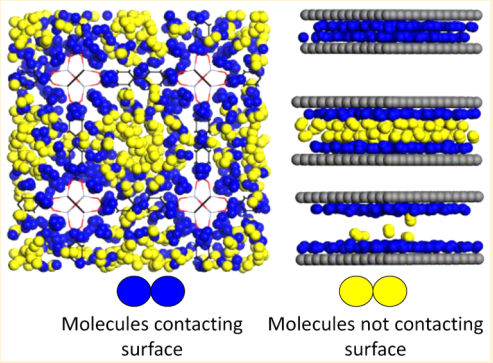

1. INTRODUCTION

Metal–organic frameworks (MOFs) are an exciting class of crystalline materials formed by inorganic "nodes" and organic "linkers" assembled into three-dimensional porous networks.[1] The structure of the network can be finely tuned by selecting an appropriate combination of inorganic and organic "building blocks."[2] This degree of structural (and property) control is unprecedented in porous-materials chemistry, and it has resulted in the intensive investigation of MOFs for applications such as separations,[3] sensing,[4] catalysis,[5] and gas storage.[2a,6] The precise structures of MOFs have also allowed the use of molecular simulations to calculate the properties of these materials both in an explanative mode and in a predictive mode.[7] Indeed, MOF properties have been calculated computationally for a large number of potential MOF structures,[8] creating useful structure–property relationships for different applications[8,9] and guiding the discovery of new MOFs.[10]

One of the most attractive aspects of MOFs is their ability to yield high specific surface areas, so this property is routinely calculated as part of MOF characterization. The experimentally determined surface area of a MOF is often compared with that calculated geometrically for its corresponding molecular model, i.e., the perfect MOF crystal. This allows one to assess the quality of the MOF sample[11] (e.g., that the structural integrity of the MOF was maintained, and all solvent molecules were removed during the pore activation process) and establish whether the maximum performance of the synthesized MOF can be expected for a given application.[11a] Such is the importance of MOF surface area that this property has been treated as a target property for materials design. For instance, in gas storage applications, materials with increasingly higher surface areas are pursued due to the correlation between this property and adsorption loadings as shown in correlations to predict hydrogen[6d,12] and methane uptakes.[6b,9c,13]

Experimentally, estimation of the surface areas of porous materials has been commonly done by applying the theory of Brunauer, Emmett, and Teller[14] (BET) to measured nitrogen isotherms: the BET calculation produces an estimate of the

Received: September 30, 2015
Published: December 11, 2015

DOI: 10.1021/jacs.5b10266
J. Am. Chem. Soc. 2016, 138, 215–224

nitrogen monolayer loading, which is in turn converted into a BET area. With hydrogen storage as motivation, in 2010 Yaghi and co-workers[15] and Hupp and co-workers[11b] reported the materials **MOF-210** and **NU-100**, with BET areas of 6240 and 6143 m^2/g, respectively. In 2012, Farha and co-workers[11c] reported **NU-110**, the material with the highest BET area reported to date (7140 m^2/g). Pursuit of ultrahigh surface area materials has continued more recently with efforts by Kaskel and co-workers,[11d] who reported **DUT-32** (BET area of 6411 m^2/g) and Farha and co-workers who reported **NU-1103**, a water-stable zirconium-based MOF with a BET area of 6552 m^2/g.[16]

Computationally, surface areas can be calculated in a manner that emulates experiments by applying the BET theory to simulated nitrogen isotherms to produce "simulated" BET areas[17] or alternatively by applying a geometrical method. In the latter, nitrogen-accessible surface areas (NASA) can be calculated geometrically by "rolling" a nitrogen-sized spherical probe[18] across the surface of the crystal structure. The low computational cost of the geometrical method makes it preferable for high-throughput screening efforts.[8] However, the relation between geometrically calculated NASAs and BET areas and the suitability of the latter as the descriptor of the true surface area of micro- and mesoporous materials such as MOFs has been a matter of debate[16,17,19] and is discussed in a recent IUPAC technical report.[20]

This debate is exacerbated by the sensitivity of BET areas to the selected pressure range used in the BET analysis. Different pressure ranges can yield different BET areas that compare differently with the corresponding NASAs. To aid in choosing the correct pressure range for the BET analysis, Rouquerol et al.[19a] suggested four "consistency criteria," and several groups[17a,19g] have emphasized the importance of using these criteria when applying the BET method in MOFs. Rouquerol et al.[19f] also noted the need to be careful when comparing BET areas to geometrically calculated NASAs. However, in earlier work by Snurr and co-workers,[17] good agreement was found between NASAs and simulated BET areas for a small set of nanoporous materials. On the other hand, in recent work,[16] we found non-negligible discrepancies between the computed NASA and the measured BET area of **NU-1103** (5646 and 6552m^2/g, respectively), while also having trouble finding a pressure range that would satisfy all four BET consistency criteria.

The issues above highlight the challenges in correctly characterizing MOFs based on their specific surface areas, either as an assessment of MOF sample quality or as a predictor of adsorption performance. This motivated us to thoroughly investigate the application of the consistency criteria for the calculation of BET areas and determine how its application, or lack thereof, impacts the relation of BET areas to NASAs for MOFs with complex pores; for example, multimodal pore size distributions, pore shapes, and pore sizes. We consider this to be a critical task since advances in MOF synthesis[21] are enabling access to materials with more complex pore structures combining a wider range of pore shapes and sizes than before in a single material. Our goal was to obtain insights into the applicability of the four consistency criteria to calculate BET areas, assess the accuracy of the monolayer loading calculation, and assess the suitability of BET areas as descriptors of "true" surface areas, which we take to be the geometrically calculated NASAs. Anticipating that the final outcome of this assessment may vary depending on the complexity and/or nature of the MOF pore structure, we sought to investigate a diverse set of MOFs in terms of pore structure and pore size. We accomplished this by investigating MOFs of differing topologies, including MOFs with the highest BET areas reported in the literature[11b−d,15,16,22] and also including graphene slit pores as representative simple pores with a unimodal pore size distribution.

2. COMPUTATIONAL METHODOLOGY

NASAs were calculated geometrically using the method described by Bae et al.,[17b] where NASAs correspond to the areas of the surface created by the center of a nitrogen-sized hard spherical probe when it is rolled over the atoms of the crystal structure of interest. The diameter of the spherical probe and the diameter of the framework atoms are equal to $2^{1/6}$ times the corresponding Lennard-Jones (LJ) "σ" parameter. The σ parameter of the spherical probe (3.32 Å) is based on the TraPPE force field of nitrogen,[23] whereas those of the atoms of the investigated materials are based on the universal force field (UFF).[24]

Calculation of BET areas was based on the linearized BET isotherm derived from the assumptions made by the BET theory:[14a]

$$\frac{P/P_0}{N(1-P/P_0)} = \frac{1}{N_m C} + \frac{C-1}{N_m C}\left(\frac{P}{P_0}\right) \quad (1)$$

The above equation relates the adsorbate loading N with the relative pressure P/P_o, where P_o is the saturation pressure of nitrogen, and C and N_m are constants. C is related to the energetics of adsorption, whereas N_m corresponds to the monolayer loading, which in turn is related to the specific surface area of the material. Based on the simulated nitrogen isotherms, the left side of eq 1 was plotted versus relative pressure, and a linear region was selected from the plot so the values of C and N_m could be extracted from linear regression. The linear region ($R^2 > 0.995$) was selected with the goal of satisfying the four BET consistency criteria proposed by Rouquerol et al.,[19a] namely:

(1) Only a range where $N(1 - P/P_o)$ increases monotonically with P/P_o should be selected.
(2) The value of C resulting from the linear regression should be positive.
(3) The monolayer loading N_m should correspond to a relative pressure P/P_o falling within the selected linear region.
(4) The relative pressure corresponding to the monolayer loading calculated from BET theory ($1/\sqrt{C+1}$) should be equal to the pressure determined in criterion 3. (For this criterion, Rouquerol et al.[19f] suggested a tolerance of 20%.)

The first and the second criteria were always satisfied in all BET area calculations reported here. However, satisfying the third and fourth criteria was more problematic. If no linear region was identified to satisfy the third and fourth criteria, then the linear region that minimized the deviation from the criteria was selected.

Simulated nitrogen adsorption isotherms at 77 K were obtained using grand canonical Monte Carlo (GCMC) using the RASPA code.[25] Consistent with the parameters used for the NASA calculation, the atoms of the adsorbent materials and the adsorbate nitrogen molecules were modeled with UFF[24] and the TraPPE force field, respectively.[23] Further details on

DOI: 10.1021/jacs.5b10266
J. Am. Chem. Soc. 2016, 138, 215−224

GCMC simulations and methods to analyze simulation "snapshots" are presented in detail in the Supporting Information.

3. RESULTS AND DISCUSSION

3.1. Graphene Slit Pores. We start by studying the application of the BET theory to characterize simple slit pores between graphene sheets. Nitrogen adsorption isotherms at 77 K were calculated for slit pores between 1.5 and 29.4 Å. The geometrically calculated NASAs and the corresponding simulated BET areas are compared in Figure 1 for different pore diameters, d. These diameters were calculated as indicated in the Supporting Information, Section S1, and account for the van der Waals radii of graphene atoms.

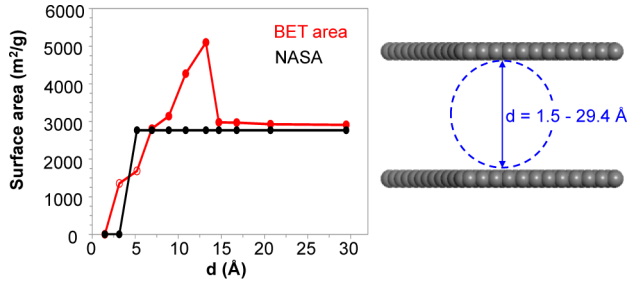

Figure 1. BET areas and geometrically calculated NASA for graphene with pore sizes in the 1.5–29.4 Å range. The empty symbols in the BET graph represent cases where not all four consistency criteria are satisfied.

For the smallest pore diameter, d = 1.5 Å, neither nitrogen molecules modeled with the TraPPE force field nor the hard nitrogen-sized spherical probe are able to access the pores. At d = 3.2 Å, only the "soft" TraPPE nitrogen molecules are able to access the pores (but not the "rigid" spherical probe), resulting in a simulated BET area of ~1300 m²/g, although the NASA is zero. When the pores are large enough (e.g., d = 5.2 Å) and accessible by the spherical probe, the NASA remains constant as the pore size increases, but the BET area presents an irregular behavior. Indeed, in agreement with a previous report,[26] depending on the pore size, the BET area can either underpredict, match, or overpredict the NASA.

Representative cases of the behavior in Figure 1 are displayed in Figure 2, corresponding to graphene pore sizes 6.9, 13.2, and 14.7 Å. Note that for these cases, the BET calculations rigorously satisfy all four consistency criteria, yet the agreement with the NASA is pore size-dependent. As we will show, this dependency mainly originates from differences between the BET-calculated monolayer loading and the "true monolayer loading." We define the true monolayer loading as the amount of nitrogen molecules contacting the pore walls at P_o (i.e., the bulk nitrogen vapor/liquid saturation pressure), which we obtain from simulations using the algorithm described in Supporting Information, Section S1. Furthermore, by applying the algorithm to calculate the number of molecules contacting the pore walls at different pressures, we can track the formation of the monolayer as illustrated by the red dashed curves in Figure 2a,c,e.

From Figure 2a, it is apparent that for d = 6.9 Å all adsorbed nitrogen molecules are in contact with the walls at all pressures. For this pore diameter, the true monolayer loading is equal to the saturation loading, which is in turn equal to the BET-predicted monolayer loading (which is given by the intersection of the vertical dashed line and the isotherm). Notably, after

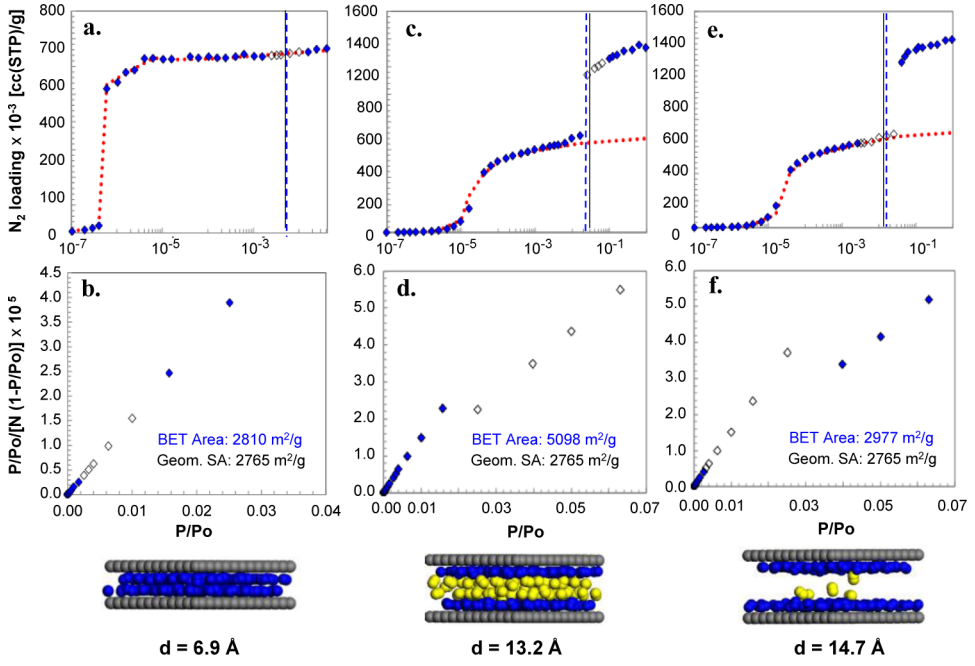

Figure 2. BET calculations that fulfill all consistency criteria, but differ in terms of agreement with the respective geometric NASAs. (a, c, and e) Nitrogen isotherms for graphene with different separation distances; red dashed curves correspond to the amount of nitrogen contacting the graphene atoms. White symbols indicate points used in BET calculation; blue vertical dashed lines indicate the P/P_o values that correspond to the BET-predicted monolayer loadings; black vertical lines indicate the values of $1/(\sqrt{C}+1)$. (b, d, and f) BET plots; all points shown satisfy the first consistency criterion; white symbols indicate points used in calculation. (a, b) d = 6.9 Å, (c, d) d = 13.2 Å, (e, f) d = 14.7 Å. The simulation snapshots correspond to the pressure of the BET-predicted monolayer loading. Atoms are shown in vdW representation (carbon atoms, gray; nitrogen atoms, blue when they are in contact with the graphene atoms and yellow when they are not).

DOI: 10.1021/jacs.5b10266
J. Am. Chem. Soc. 2016, 138, 215–224

applying the first consistency criterion, only one possible linear region for the BET calculation emerges (Figure 2b), rendering the BET area insensitive to whether or not the third and fourth BET consistency criteria are fulfilled (Figure S3.28). Similar observations apply for pore diameters of 3.2 and 5.2 Å (Figures S3.26 and S3.27).

For d = 13.2 Å, two distinct eligible linear regions with different slopes appear after applying the first consistency criterion (Figure 2d). Comparison with the isotherm in Figure 2c shows that the first and second linear regions correspond to the first and second isotherm steps, which, respectively, correspond to the completion of the monolayer and pore filling. However, the second linear region (pore filling) is the one that fulfills all four BET consistency criteria, which leads to the overestimation of the monolayer loading. The snapshot for d = 13.2 Å in Figure 2, taken at the pressure corresponding to the BET-predicted monolayer loading, shows that the overestimation of the monolayer occurs by incorrectly including noncontacting molecules (in yellow). Selecting a pressure interval in the first linear region would result in BET-predicted monolayer loadings closer to the true one, consequently improving the agreement between the BET area (2700−3100 m^2/g) and the NASA (2765 m^2/g) (see Figure S3.31). Yet it was not possible to select an interval in the first linear region that would satisfy either the third or fourth criterion. For this pore diameter, it is clear that the BET theory fails to distinguish between monolayer formation and pore filling. We denote this as "pore-filling contamination" in the BET area calculation.

As the pore diameter increases, pore-filling contamination stops being an issue. For instance, for d = 14.7 Å, again two eligible linear regions emerge after applying the first consistency criterion (Figure 2f). As before, these two regions correspond to the steps in the isotherm (Figure 2e). However, for this pore diameter, the first linear range does fulfill all four consistency criteria, and the BET-predicted monolayer loading agrees with the true monolayer loading (see snapshot for d = 14.7 Å in Figure 2), which also leads to good agreement with the NASA.

3.2. Metal−Organic Frameworks. With the insights obtained in Section 3.1 for simple pores, we now proceed to analyze metal−organic frameworks (MOFs). The investigated MOFs have different pore structures as a result of having different topologies and organic linkers of different sizes, see Figure 3. (For structural details of the studied MOFs, see Supporting Information, Section S2.)

For the **pcu** topology we investigated **IRMOF-1**,[2a] **IRMOF-10**,[2a] **IRMOF-16**,[2a] and the hypothetical MOF **pcu**-*PPPP* ("pcu" before the dash indicates the topology, and the four "*P*"s after the dash indicate that the MOF is based on linkers constituted by four consecutive phenyl rings). These **pcu** MOFs possess two relatively similar types of pores and are based on Zn_4O nodes coordinated by six ditopic linkers each. For the **fcu** topology we studied **UiO-66**,[27] **UiO-67**,[27] **NU-800**,[10] **UiO-68**,[27] and the hypothetical structure **fcu**-*PPPP*. These **fcu** MOFs feature two types of pores (octahedral and tetrahedral cages) and are based on Zr_6O_8 nodes coordinated by 12 ditopic linkers each. For the **ftw** topology, we investigated **MOF-525**,[28] **NU-1100**,[29] **NU-1101**,[16] **NU-1102**,[16] **NU-1103**,[16] and **NU-1104**.[16] These **ftw** MOFs have two types of pores (cubic and octahedral cages) and are based on Zr_6O_8 nodes coordinated by 12 tetratopic linkers each. For the **rht** topology, we analyzed **PCN-61**,[30] **NOTT-112**,[31] **NU-111**,[32] **NU-100**,[11b] **NU-109**,[11c] and **NU-110**.[11c] These **rht** MOFs feature four types of pores and are based on supermolecular cages based on copper paddlewheels ($[Cu_2(COO)_4]_{12}[C_4H_4]_{24}$) coordinated by 24 hexatopic linkers each. Since the materials listed above include MOFs reported to have record-high BET areas, we also studied, for completeness, other MOFs that have been reported with similarly high BET areas: **MOF-177**,[22a] **MOF-210**,[15] **DUT-32**,[11d] and **DUT-49**.[22b]

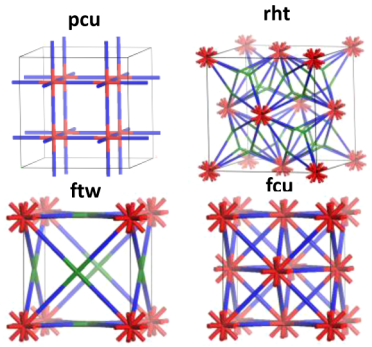

Figure 3. Schematics of the topologies for the MOFs investigated in this work. **pcu**: **IRMOF-1**, **IRMOF-10**, **IRMOF-16**, **pcu**-*PPPP*; **rht**: **PCN-61**, **NOTT-112**, **NU-111**, **NU-100**, **NU-109**, **NU-110**; **ftw**: **MOF-525**, **NU-1100**, **NU-1101**, **NU-1102**, **NU-1103**, **NU-1104**; **fcu**: **UiO-66**, **UiO-67**, **NU-800**, **UiO-68**, **fcu**-*PPPP*. Additionally, **qom** **MOF-177**, **umt** **MOF-210**, **ubt** **DUT-49**, and **umt** **DUT-32** were investigated.

We start our analysis by calculating the BET areas of all MOFs from their simulated nitrogen adsorption isotherms and comparing the BET areas with the corresponding geometrically calculated NASAs. We reiterate that for the BET calculation, we sought linear regions that meet all BET criteria or that otherwise minimize the deviation from the BET criteria as noted in the methods section.

3.2.1. Calculation of BET Areas and Comparison to NASAs. Scenario 1: Rigorous Fulfillment of BET Consistency Criteria Achieved. Similar to Figure 2, Figure 4 shows that even if all BET consistency criteria are rigorously met there can be disagreement between BET area and NASAs. This is shown in Figure 4a,b for **NU-110** (the synthesized material with the highest NASA to date) where the simulated BET area overestimates the NASA of **NU-110** by ∼33% even though the linear region used in the BET calculation (white points: $0.11 < P/P_o < 0.16$) meets all consistency criteria: Note that the blue vertical dashed line ($P/P_o = 0.115$), indicating the pressure for the BET-predicted monolayer, falls within the linear range used for the calculation and that this pressure is close (within 20%) to "$1/\sqrt{C} + 1$." It is noteworthy that the pressure corresponding to the predicted monolayer loading is in a part of the isotherm where the nitrogen loading rises steeply with pressure (Figure 4a). There are other linear ranges that would result in a BET area closer to the NASA, but they would lead to deviations from the BET criteria. For instance, for the range $0.05 < P/P_o < 0.10$, the BET area would overestimate the NASA by only ∼16%, but would not meet the third and fourth criteria. This "paradox" is not unlike that discussed for graphene slit pores of 13.2 Å (Figure 2c,d).

IRMOF-1 (Figure 4 c,d) and **pcu**-*PPPP* (Figure 4 e,f) are other examples where all four criteria are fulfilled in the BET calculation. However, for **IRMOF-1** and **pcu**-*PPPP*, the BET areas match and underestimate, respectively, the corresponding NASAs. From the three examples illustrated in Figure 4 (and the three examples illustrated in Figure 2), one can conclude

DOI: 10.1021/jacs.5b10266
J. Am. Chem. Soc. 2016, 138, 215−224

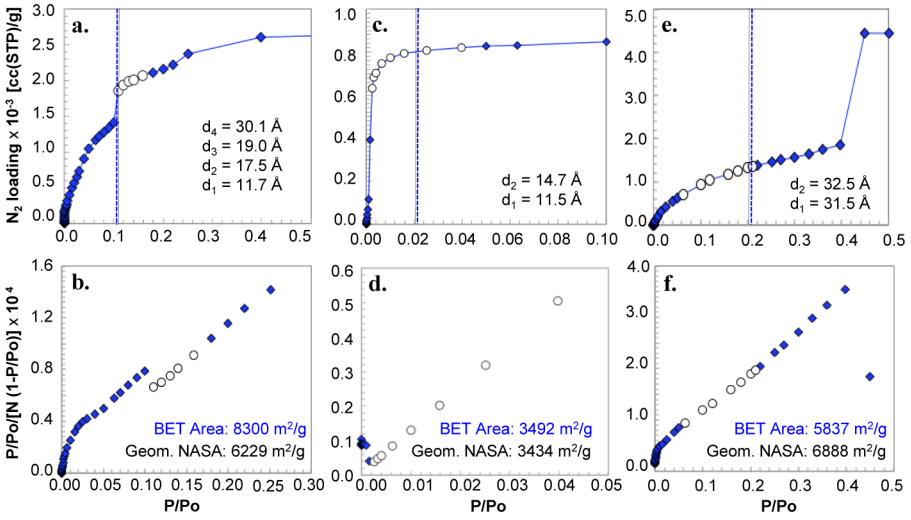

Figure 4. Example BET calculations that all fulfill all consistency criteria but differ in terms of agreement with the respective geometric NASAs. (a, c, and e) Nitrogen isotherms. White symbols indicate points used in calculation; blue vertical dashed lines indicate the P/P_o values that correspond to the calculated monolayer loadings; black vertical lines indicate the values of $1/(\sqrt{C}+1)$; inset numbers correspond to geometrically calculated pore diameters. (b, d, and f) BET plots used for the calculations; all points shown satisfy the first consistency criterion; white symbols indicate points used in calculation. (a, b) **NU-110**, (c, d) **IRMOF-1**, (e, f) **pcu**-*PPPP* (a hypothetical MOF).

that agreement between the BET area and the NASA of a given MOF is not guaranteed by fulfilling all consistency criteria during the BET calculation.

Scenario 2: Partial Fulfillment of Consistency Criteria Achieved. On the other hand, as we have noted, there may be cases where it is not possible to fulfill all four consistency criteria. In such cases it is important to minimize the deviation from the criteria, at least for consistency, if nothing else. Note, however, that minimizing the deviations one can still in some cases correctly predict the monolayer loading and find good agreement between BET areas and NASAs (e.g., see **UiO-67** in Figure S3.2).

Let us inspect some cases where fulfilling all four criteria was not possible. Figure 5 shows the case of **UiO-66**. Note that

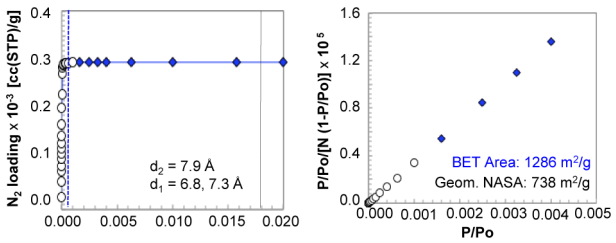

Figure 5. BET calculation for **UiO-66** (see Figure 2 for description of plots). After applying the first consistency criterion, only one linear region is left for the calculation (right). However, it was not possible to satisfy all criteria (left).

after applying the first consistency criterion only one eligible linear region emerged for the BET calculation (Figure 5 right). Similar to graphene with pores of 6.9 Å (Figure 2a,b), there is not much room to maneuver toward fulfilling the remaining BET criteria. However, unlike the graphene system, where all criteria were fulfilled, for **UiO-66** it was not possible to satisfy the fourth criterion. In the best scenario for **UiO-66**, "$1/\sqrt{C}+1$" is over 300% higher than the pressure corresponding to the BET-predicted monolayer, although the calculated BET area is essentially insensitive to whether the remaining BET criteria are fulfilled.

However, since in many MOFs the BET area does vary significantly depending on the linear region selected for the calculation, we re-emphasize that every effort should be made to select a range for the BET calculation that fulfills all criteria or that minimizes the deviation from all criteria. This engenders consistency that allows the use of BET areas to compare the quality of two experimental samples of the same MOF or to compare the quality of a MOF sample in the lab with respect to an idealized MOF crystal. Since even fulfilling all consistency criteria does not guarantee agreement between BET areas and NASAs, for rigorous determination of MOF sample quality experimental BET areas should be compared with BET areas from simulated N_2 isotherms and not with NASAs.

The basis for the above statement is that simulated nitrogen isotherms usually agree well with experimental ones when the MOF sample is well activated, so consistent application of BET theory to both isotherms should yield similar results. On the other hand, if there is a disagreement between BET area and NASA, inaccurate conclusions about the quality of the MOF sample may arise. Consider, for instance, **NU-1103** (Figure S3.10) with a NASA of 5646 m^2/g. Now imagine that an **NU-1103** sample in the lab has an experimental BET area of ~5600 m^2/g. Without further information, one would conclude that the **NU-1103** sample was optimally synthesized and activated. However, the simulated BET area of **NU-1103** is 6820 m^2/g, and it suggests that it should be possible to obtain a higher quality **NU-1103** sample. Indeed, in previous experimental work[16] we were able to adjust the synthesis and activation of **NU-1103** to obtain a BET area of 6520 m^2/g.

Summary of Overall Trends. Figure 6 shows a global perspective for all the structures investigated in this work. The shown parity plot compares the BET areas with the corresponding NASAs, also indicating whether the BET calculations meet all consistency criteria (solid symbols) or not (empty symbols). It is apparent that, for structures with NASAs in the intermediate ~2500−5000 m^2/g range, the BET areas and NASAs tend to agree well independently of whether the third and fourth consistency criteria are met (provided that deviations were minimized) and independently of the topology

DOI: 10.1021/jacs.5b10266
J. Am. Chem. Soc. 2016, 138, 215−224

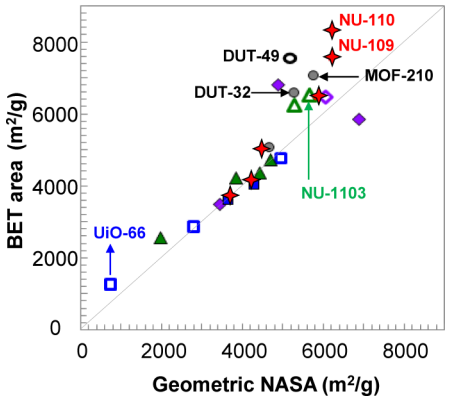

Figure 6. BET area versus geometric surface area calculated for MOFs of various topologies: **pcu** (diamonds), **fcu** (squares), **ftw** (triangles), **rht** (stars), and other topologies (circles). For MOFs whose BET calculation fulfilled all consistency criteria filled symbols are used (open symbols otherwise). Other topologies correspond to **MOF-177**, **MOF-210**, **DUT-32**, and **DUT-49**.

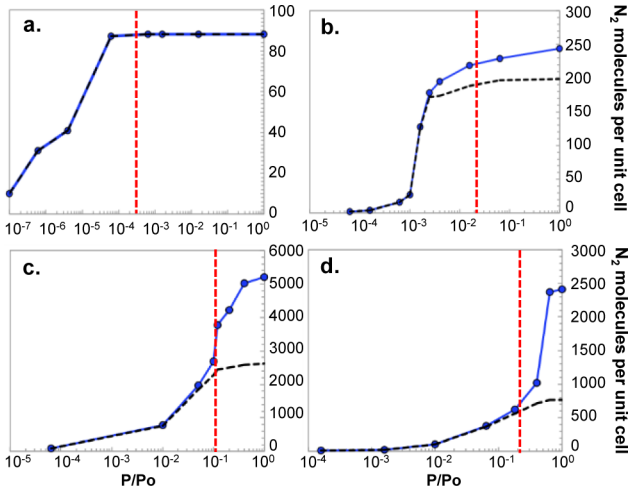

Figure 7. Breakdown of total number of nitrogen molecules adsorbed (blue solid curve) and number of nitrogen molecules in contact with pore walls (black dashed curve) for MOFs discussed in Figures 4 and 5: (a) **UiO-66**, (b) **IRMOF-1**, (c) **NU-110**, and (d) **pcu**-*PPPP*. The dashed black curve tracks the formation of the monolayer. The vertical line indicates the pressure corresponding to the formation of the monolayer based on the BET calculation.

of the MOF. On the other hand, BET areas tend to overestimate the corresponding NASAs for structures with geometrically calculated NASAs in the ranges of 0−2500 and 5000−6500 m^2/g. The overestimation in the lower NASA range is low in absolute terms (e.g., 500 m^2/g for **UiO-66**) but can be high in percent terms (e.g., ∼74% for **UiO-66**). The overestimation in the higher NASA range can be significantly higher in absolute terms (e.g., ∼2000 m^2/g for **NU-110**), but not as high in percent terms (e.g., ∼33% for **NU-110**).

3.2.2. Molecular Simulation Insights into the Formation of the Monolayer. True Monolayer Loading and Pore Filling Contamination. We now discuss true monolayer loading and pore-filling contamination for the materials considered in Figures 4 and 5. We analyzed the molecule positions during the simulations and counted the number of molecules in contact with the surface using the algorithm described in Supporting Information, Section S1, to track the formation of the monolayer. Figure 7 shows the monolayer formation (dashed curves) and full isotherms (solid curves) for these materials. Note that the difference between the two curves represents the nitrogen molecules not contacting the pore walls, and therefore corresponding to pore filling.

For **UiO-66** in Figure 7a (a material with "small" micropores, i.e., d < 10 Å, that is expected to fill with nitrogen through a pore-filling mechanism), all nitrogen molecules contact the pore surface. Not surprisingly, although all four criteria are not fulfilled, the BET calculation for **UiO-66** correctly predicts a monolayer loading (see intersection of vertical line and the solid curve) that it is equal to the nitrogen saturation loading. Indeed, it is interesting that despite the correct estimation of the monolayer loading, the BET area of **UiO-66** (1286 m^2/g) disagrees with the NASA (736 m^2/g). This difference arises because there are regions nonaccessible for the hard spherical probe, but that are accessible for the soft nitrogen molecule, as discussed at the end of this subsection. It is worth recalling that the **UiO-66** analyzed here is a perfect crystal, unlike typical synthesized **UiO-66** crystals, which present defects such as missing linkers. Thus, here the higher BET area of UiO-66 relative to the NASA is not related to crystal defects.

For **IRMOF-1** and **NU-110** (Figure 7b,c), the pressure for monolayer completion from the BET calculation is a good approximation of the true pressure, where the monolayer is completed (see the intersection of the vertical line with the dashed curve). For instance, for **IRMOF-1** and **NU-110**, the amount of pore-contacting molecules at this pressure corresponds to 96% and 93% of the true monolayer loadings of these MOFs, respectively. The caveat is that at this pressure pore-filling has already started to occur (see the separation of the solid and dashed curves), so molecules that are not contacting the pore walls are erroneously counted by the BET calculation as contributing to the monolayer. For **IRMOF-1**, the BET calculation overestimates the true monolayer loading only by ∼10%, whereas for **NU-110** it does so by ∼40%. On the other hand, for **pcu**-*PPPP* (which has only mesoporous cages (d ∼ 32−33 Å), Figure 7d), the BET calculation correctly predicts the true monolayer loading within a ∼1% error.

The parity plot in Figure 8 summarizes how close the BET-predicted monolayer loadings are to the true monolayer loadings in all MOFs investigated in this work. Notice that the BET theory makes a fair prediction of the true monolayer loadings of MOFs for values lower than ∼1000 cc(STP)/g. On the other hand, the BET theory tends to overestimate the monolayer loading of the studied structures for which this loading takes values higher than ∼1000 cc(STP)/g (with the exception of **pcu**-*PPPP*). Structures with significant overestimation of the monolayer loading (≥20%) include **DUT-49**, **NU-110**, **NU-109**, **DUT-32**, **MOF-210**, **NU-1103**, and **IRMOF-10**.

If the monolayer loadings are significantly overestimated, it is expected that the BET areas of the relevant structures will be significantly higher than the corresponding NASAs. Thus, a related question arises: How close would the BET areas and NASAs be if it were possible to accurately estimate the monolayer loading from the nitrogen isotherms? To address this question, we calculated the true monolayer loadings of all structure from simulation snapshots. Then, we used these values and converted to surface area values just as one would with the BET-predicted monolayer loadings. Figure 9 compares the surface areas calculated from the true monolayer loadings to the NASAs.

DOI: 10.1021/jacs.5b10266
J. Am. Chem. Soc. 2016, 138, 215−224

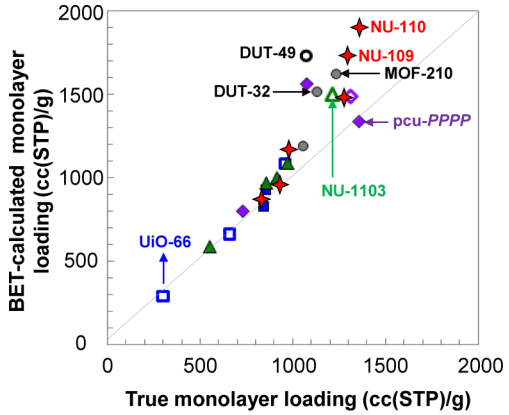

Figure 8. BET-calculated monolayer loading versus true monolayer loading obtained from analysis of simulation snapshots for MOFs of various topologies: **pcu** (diamonds), **fcu** (squares), **ftw** (triangles), **rht** (stars), other topologies (circles). For MOFs whose BET calculation fulfilled all consistency criteria, filled symbols are used (open symbols otherwise). Other topologies correspond to **MOF-177**, **MOF-210**, **DUT-32**, and **DUT-49**.

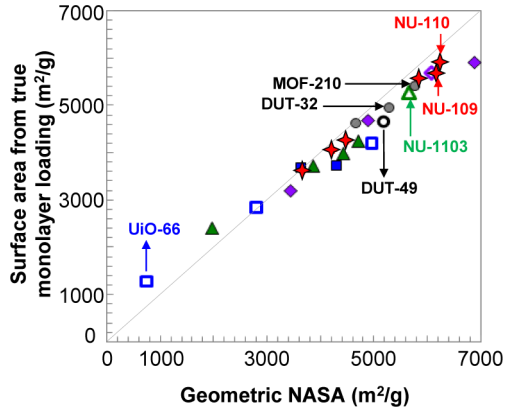

Figure 9. Surface area calculated from true monolayer loading versus geometrically calculated NASA for MOFs of various topologies: **pcu** (diamonds), **fcu** (squares), **ftw** (triangles), **rht** (stars), other topologies (circles). For MOFs whose BET calculation fulfilled all consistency criteria, filled symbols are used (open symbols otherwise). Other topologies correspond to **MOF-177**, **MOF-210**, **DUT-32**, and **DUT-49**.

It is apparent that the parity plot in Figure 9 is a significant improvement over that in Figure 6, most notably for MOFs with NASAs in the ~5000−6500 m^2/g range. For instance, the comparison of surface areas calculated from true monolayer loadings and NASAs is 5900 vs 6230 m^2/g for **NU-110**, 5400 vs 5800 m^2/g for **MOF-210**, 5270 vs 5650 m^2/g for **NU-1103**, 4930 vs 5300 m^2/g for **DUT-32**, and 4900 m^2/g vs 4680 m^2/g for **IRMOF-10**. Notice that for the listed MOFs, the surface areas derived from true monolayer loadings are somewhat lower than the corresponding NASAs. Based on Figure 9, this occurs for MOFs with NASAs higher than ~3000 m^2/g, which may indicate a somewhat less efficient packing of nitrogen molecules in the monolayer contacting the pore walls than what it is assumed in converting the monolayer loading to a surface area.

On the other hand, for MOFs with NASAs lower than ~2500 m^2/g such as the previously discussed **UiO-66** (1290 vs 740 m^2/g) and **MOF-525** (2410 vs 1980 m^2/g), the surface areas calculated from true monolayer loadings tend to overestimate the corresponding NASAs. This suggests the presence of regions in these MOFs that are inaccessible for the nitrogen-sized hard spherical probe used in the geometrical calculation of NASAs, but that are accessible by the soft nitrogen molecules used in the GCMC simulations (see example for **UiO-66** in Figure S6.1) This is similar to the results for the graphene layers with a 3.2 Å pore diameter where the BET area had a finite value, while the NASA was zero (second point in Figure 1).

Breakdown of Adsorption Loadings by Cage Types. At this point it is clear that the BET theory overestimates the monolayer loading when it is not able to distinguish between the ending of monolayer formation and the beginning of pore filling, a situation we refer to as "pore-filling contamination". For instance, this occurs for simple graphene-based slit pores (e.g., for d = 13.2 Å). Yet, the simplicity of the pore of these systems allows one to recognize a linear range that would yield the true monolayer even if it does not satisfy all consistency criteria (Figure S3.31). For MOFs, pore-filling contamination can be especially pronounced when there are cages of different sizes, which fill at different pressure ranges, as we will now demonstrate.

For MOFs of **fcu**, **ftw**, **pcu**, and **rht** topologies, we analyzed the simulation snapshots at different pressures and assigned the adsorbed molecules to the different cage types characteristic of each topology. Figure 10 breaks down by cages both the total

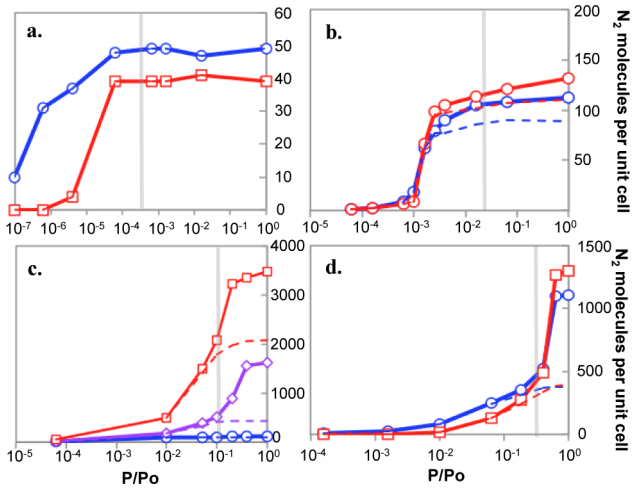

Figure 10. Breakdown of total number of nitrogen molecules adsorbed (solid curves) and number of nitrogen molecules in contact with pore walls (dashed curves) for MOFs discussed in Figure 4 and 5: (a) **UiO-66** (blue: d = 6.9, 7.3 Å; red: d = 7.9 Å), (b) **IRMOF-1** (blue: d = 11.5 Å; red: d = 14.7 Å, (c) **NU-110** (blue: d = 11.7 Å; red: d = 17.5, 19.0 Å; purple: d = 30.1 Å), and (d) **pcu**-*PPPP* (blue d = 32 Å, red d = 33 Å). The dashed curves track the formation of the monolayer in each cavity. The vertical line indicates the pressure corresponding to the formation of the monolayer based on the BET calculation.

amount of adsorbed nitrogen (solid curves) and the molecules in contact with the pore walls (dashed lines) for the four MOFs discussed in Figure 7 (i.e., **UiO-66**, **IRMOF-1**, **NU-110**, and **pcu**-*PPPP*). The amount of pore filling for each cage type is given by the difference between the corresponding solid and dashed lines at the pressure of interest.

For **UiO-66** (Figure 10a), the tetrahedral cages (blue curve) start to fill at lower pressures than the octahedral cages (red curve). Comparison with Figure 7a shows that the step in the

DOI: 10.1021/jacs.5b10266
J. Am. Chem. Soc. 2016, 138, 215−224

Table 1. Contribution of Mesopore and Micropore Volumes to the Total Pore Volume for the Investigated MOFs along with Information on Topology, BET Area, Fulfillment of BET Criteria, Geometrically Calculated NASA, and NASA-Based Ranking

MOF	mesop. volume d > 20 Å	microp. volume d < 20 Å		topology	BET area (m^2/g)	NASA (m^2/g)	BET criteria fulfilled?	NASA-based ranking
		d > 10 Å	d < 10 Å					
UiO-66	0%	0%	100%	**fcu**	1290	740	no	25
UiO-67	0%	36%	64%	**fcu**	2900	2800	no	23
NU-800	0%	30%	70%	**fcu**	3645	3600	yes	21
UiO-68	0%	50%	50%	**fcu**	4020	4300	yes	17
fcu-*PPPP*	68%	32%	0%	**fcu**	4750	4950	no	11
MOF-525	0%	58%	42%	**ftw**	2560	1980	yes	24
NU-1100	0%	54%	46%	**ftw**	4200	3860	yes	19
NU-1101	0%	35%	64%	**ftw**	4350	4420	yes	16
NU-1102	47%	53%	0%	**ftw**	4730	4710	yes	13
NU-1103	44%	56%	0%	**ftw**	6860	5650	no	7
NU-1104	47%	53%	0%	**ftw**	6270	5290	no	9
IRMOF-1	0%	100%	0%	**pcu**	3490	3430	yes	22
IRMOF-10	54%	46%	0%	**pcu**	6700	4900	yes	12
IRMOF-16	100%	0%	0%	**pcu**	6500	6060	no	4
pcu-*PPPP*	100%	0%	0%	**pcu**	5837	6888	yes	1
PCN-61	0%	60%	40%	**rht**	3780	3700	yes	20
NOTT-112	48%	52%	0%	**rht**	4160	4240	yes	18
NU-111	40%	60%	0%	**rht**	5050	4500	yes	15
NU-100	42%	58%	0%	**rht**	6460	5820	yes	5
NU-109	35%	65%	0%	**rht**	7552	6180	yes	3
NU-110	32%	68%	0%	**rht**	8310	6230	yes	2
DUT-32[a]	yes	yes	–	**umt**	6582	5300	yes	8
DUT-49[a]	yes	yes	–	**ubt**	7550	5176	no	10
MOF-210[a]	yes	yes	–	**umt**	7060	5800	yes	6
MOF-177[a]	–	yes	–	**qom**	5159	4673	yes	14

[a]For MOFs that are not of **fcu**, **ftw**, **pcu**, or **rht** topology, we only state whether there is micropore or mesopore contribution to the pore volume based on the calculated pore size distribution.

UiO-66 isotherms ($P/P_o \sim 4.0 \times 10^{-6}$) is due to a steep rise in the loading of the octahedral cages, although at this pressure the tetrahedral cages are not completely filled. Moreover, the curves for both the tetrahedral and octahedral cages plateau at the same pressure ($P/P_o \sim 6.3 \times 10^{-5}$), indicating that both types of cavities finish filling simultaneously. For **IRMOF-1** (Figure 10b) and **pcu**-*PPPP* (Figure 10d), their two types of cavities (large (red) and small (blue)) behave rather similarly, although the small cavities start to fill slightly faster, and the large cavities host a slightly larger number of molecules at the saturation point. For **IRMOF-1**, however, the small cavities curve has a somewhat less steep rise after $P/P_o \sim 0.001$ and somewhat more pore-filling contamination at the pressure corresponding to the BET-predicted monolayer loading (vertical line) than the large cavity.

For **NU-110**, Figure 10c shows that the small cages (blue curve, d = 11.7 Å), the tetrahedral and interstitial cages (red curve, d = 17.5 and 19.0 Å), and the octahedral cages (purple curve, d = 30.1 Å) take up nitrogen simultaneously up to $P/P_o \sim 0.01$, with all molecules contacting the pore walls. Inspection of simulation snapshots at this pressure reveals that the nitrogen molecules go to the tight corners of the octahedral, tetrahedral, and interstitial cages and that the small cages are completely filled (indeed the blue curve plateaus at $P/P_o \sim 0.01$). Incorporation of nitrogen molecules into the monolayer continues for all other cages up to $P/P_o \sim 0.05$, but as the pressure increases further, the monolayer formation regime continues only for the octahedral cages, while both pore filling and monolayer formation occur for the tetrahedral and interstitial cages. At the pressure that the monolayer formation ends for the octahedral cages, which approximately corresponds to the pressure for the BET-predicted monolayer loading (vertical line in Figure 10c), there is already a significant amount of pore filling (i.e., noncontacting molecules) in the tetrahedral and interstitial cavities that is erroneously counted in the BET-predicted monolayer loading. Notice that although the small cage fills at low pressure, it does not contribute to the overestimation of the true monolayer loading because all molecules in such cages contact the pore walls.

Based on the adsorption loading breakdown by cavities for **NU-110** and also other MOFs (Figures S5.1–S5.4), it can be seen that the amount of overestimation of the monolayer loading in MOFs depends on the sizes of the different cages and the relative contribution of each cage to the total pore volume. Table 1 uses the adsorption breakdown information at the saturation point (P/P_o = 1.0) and the sizes of the different cages to determine the percentage of mesopore ($d \geq 20$ Å) and micropore (d < 20 Å) volume in each structure. The micropore volume percentage is further split into the contribution of "small" micropores ($d \leq 10$ Å) and "large" micropores (d > 10 Å), where the $d \sim 10$ Å threshold is a simple symmetric choice (as a reference, IUPAC classifies micropores as "ultra-micropores," d < 7.0 Å, and "supermicropores," d > 7.0 Å). For completeness, Table 1 also lists the topology of the investigated structures, their BET areas and whether the BET calculation satisfied all criteria, and their nitrogen-accessible surface area (NASAs) with their ranking based on this property. Using the data presented in Table 1, we now discuss the

DOI: 10.1021/jacs.5b10266
J. Am. Chem. Soc. 2016, 138, 215–224

dependency of BET area calculations on the diversity of pore sizes in the studied structures.

Summary of Overall Trends. To summarize how the combination of different pore sizes affects the BET area calculation and its comparability with the geometrically calculated NASA, Figure 11 plots the second largest cage size versus the largest cage size for all 25 MOFs investigated here. The size of the point for each MOF in the plot is proportional to the absolute deviation between the BET area and NASA. The graph illustrates that the most significant deviations between BET areas and NASAs tend to occur for structures that feature both mesopores ($d \geq 20$ Å) and large micropores (10 Å $\leq d \leq$ 20 Å) in a given pore structure. This occurs due to the overlap of the pore-filling and monolayer formation "regimes" of each type of pore combined with the fact that the pores are large enough that pore-filling contamination can be significant.

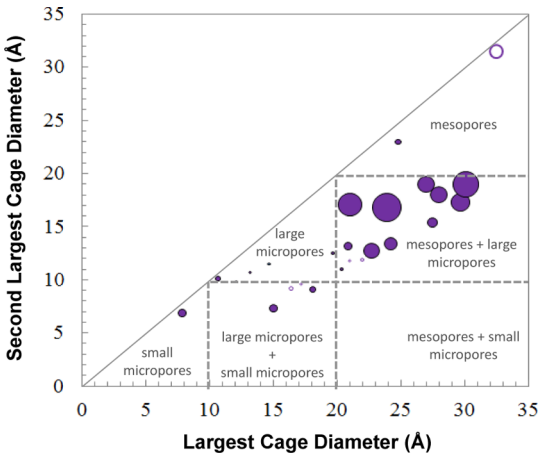

Figure 11. Second largest cage diameter versus largest cage diameter for all MOFs investigated in this work. Each point corresponds to one structure, where the point size is proportional to the absolute deviation between the BET area and the geometric NASA (maximum deviation was 2080 m^2/g for the MOF with the highest NASA, 6290 m^2/g, **NU-110**). Filled points for BET area > NASA and unfilled points for BET area < NASA.

4. CONCLUSIONS

For a wide variety of MOFs, we simulated nitrogen adsorption isotherms and calculated BET areas from the simulated isotherms by applying the four consistency criteria proposed by Rouquerol et al., and we compared the BET areas with NASAs calculated geometrically from the crystal structures. Through analysis of simulation snapshots, we were able to directly discern monolayer formation and pore filling for different cages in each material. From these results, we conclude the following: (1) BET calculations that fulfill all consistency criteria can still overestimate the true monolayer loading (e.g., **NU-110**). (2) The extent of agreement between BET areas and NASAs does not depend on whether the BET consistency criteria are strictly fulfilled (e.g., **UiO-67**). (3) Determination of the true monolayer loadings improves dramatically the extent of agreement between nitrogen adsorption-derived surface areas and NASAs; thus the main challenge in using BET areas for MOFs is to accurately estimate the true monolayer loading. (4) The true monolayer loading of MOFs completely constituted by small pores (d < 10 Å) is equal to the saturation loading. (5) Overestimation of true monolayer loadings during BET calculations tends to be more significant for structures that combine mesopores ($d \geq 20$ Å) and large micropores (d = 10–20 Å). (6) Rigorous surface-area-based assessment of the quality of a MOF sample should be done by comparing its experimental BET area to its simulated BET area, not to its NASA, making sure that the four BET consistency criteria are used to select the pressure range for the BET calculations. (7) Although "ultrahigh surface area" MOFs reported to date tend to suffer from overestimation of their true monolayer loadings in BET calculations, the surface areas derived from their true monolayer loadings as well as their NASAs are still remarkably high (assuming complete activation): 5913 m^2/g for **NU-110** (NASA = 6229 m^2/g), 5542 m^2/g for **NU-100** (5822 m^2/g), 5396 m^2/g for **MOF-210** (5770 m^2/g), 5273 m2/g for **NU-1103** (5650 m^2/g), and 4933 m^2/g for **DUT-32** (5297 m^2/g).

■ ASSOCIATED CONTENT

Supporting Information

The Supporting Information is available free of charge on the ACS Publications website at DOI: 10.1021/jacs.5b10266.

Detailed computational methods; cage types by topology; detailed BET calculations; curves tracking the formation of the monolayer; curves breaking down adsorption loading by cage types (PDF)

■ AUTHOR INFORMATION

Corresponding Author

*snurr@northwestern.edu

Author Contributions

‖These authors contributed equally.

Notes

The authors declare the following competing financial interest(s): Omar Farha, Joseph Hupp, and Randall Snurr have a financial interest in the start-up company NuMat Technologies, which is seeking to commercialize MOFs.

■ ACKNOWLEDGMENTS

The work presented herein was funded by the National Science Foundation award number DMR-1334928. The computations were made possible by the high-performance computing system, QUEST, at Northwestern University and the NERSC computing resources of the U.S. Department of Energy.

■ REFERENCES

(1) (a) Kim, J.; Chen, B.; Reineke, T. M.; Li, H.; Eddaoudi, M.; Moler, D. B.; O'Keeffe, M.; Yaghi, O. M. *J. Am. Chem. Soc.* **2001**, *123*, 8239. (b) Horike, S.; Shimomura, S.; Kitagawa, S. *Nat. Chem.* **2009**, *1*, 695.

(2) (a) Eddaoudi, M.; Kim, J.; Rosi, N.; Vodak, D.; Wachter, J.; O'Keeffe, M.; Yaghi, O. M. *Science* **2002**, *295*, 469. (b) Zhao, D.; Timmons, D. J.; Yuan, D.; Zhou, H.-C. *Acc. Chem. Res.* **2011**, *44*, 123.

(3) (a) Snurr, R. Q.; Hupp, J. T.; Nguyen, S. T. *AIChE J.* **2004**, *50*, 1090. (b) Sumida, K.; Rogow, D. L.; Mason, J. A.; McDonald, T. M.; Bloch, E. D.; Herm, Z. R.; Bae, T.-H.; Long, J. R. *Chem. Rev.* **2012**, *112*, 724. (c) Li, J.-R.; Sculley, J.; Zhou, H.-C. *Chem. Rev.* **2012**, *112*, 869. (d) Holcroft, J. M.; Hartlieb, K. J.; Moghadam, P. Z.; Bell, J. G.; Barin, G.; Ferris, D. P.; Bloch, E. D.; Algaradah, M. M.; Nassar, M. S.; Botros, Y. Y.; Thomas, K. M.; Long, J. R.; Snurr, R. Q.; Stoddart, J. F. *J. Am. Chem. Soc.* **2015**, *137*, 5706.

(4) (a) Kreno, L. E.; Leong, K.; Farha, O. K.; Allendorf, M.; Van Duyne, R. P.; Hupp, J. T. *Chem. Rev.* **2012**, *112*, 1105. (b) Yamagiwa,

DOI: 10.1021/jacs.5b10266
J. Am. Chem. Soc. 2016, 138, 215–224

H.; Sato, S.; Fukawa, T.; Ikehara, T.; Maeda, R.; Mihara, T.; Kimura, M. *Sci. Rep.* **2014**, *4*, 6247.
(5) Liu, J.; Chen, L.; Cui, H.; Zhang, J.; Zhang, L.; Su, C.-Y. *Chem. Soc. Rev.* **2014**, *43*, 6011.
(6) (a) Rosi, N. L.; Eckert, J.; Eddaoudi, M.; Vodak, D. T.; Kim, J.; O'Keeffe, M.; Yaghi, O. M. *Science* **2003**, *300*, 1127. (b) Düren, T.; Sarkisov, L.; Yaghi, O. M.; Snurr, R. Q. *Langmuir* **2004**, *20*, 2683. (c) Wong-Foy, A. G.; Matzger, A. J.; Yaghi, O. M. *J. Am. Chem. Soc.* **2006**, *128*, 3494. (d) Frost, H.; Snurr, R. Q. *J. Phys. Chem. C* **2007**, *111*, 18794. (e) Zhou, W.; Wu, H.; Hartman, M. R.; Yildirim, T. *J. Phys. Chem. C* **2007**, *111*, 16131. (f) Peng, Y.; Krungleviciute, V.; Eryazici, I.; Hupp, J. T.; Farha, O. K.; Yildirim, T. *J. Am. Chem. Soc.* **2013**, *135*, 11887.
(7) (a) Yang, Q.; Zhong, C. *J. Phys. Chem. B* **2005**, *109*, 11862. (b) Greathouse, J. A.; Allendorf, M. D. *J. Am. Chem. Soc.* **2006**, *128*, 10678. (c) Yang, Q.; Xue, C.; Zhong, C.; Chen, J.-F. *AIChE J.* **2007**, *53*, 2832. (d) Liu, D.; Zhong, C. *J. Mater. Chem.* **2010**, *20*, 10308. (e) Getman, R. B.; Bae, Y.-S.; Wilmer, C. E.; Snurr, R. Q. *Chem. Rev.* **2012**, *112*, 703. (f) Haldoupis, E.; Nair, S.; Sholl, D. S. *J. Am. Chem. Soc.* **2012**, *134*, 4313.
(8) Wilmer, C. E.; Leaf, M.; Lee, C. Y.; Farha, O. K.; Hauser, B. G.; Hupp, J. T.; Snurr, R. Q. *Nat. Chem.* **2012**, *4*, 83.
(9) (a) Lin, L.-C.; Berger, A. H.; Martin, R. L.; Kim, J.; Swisher, J. A.; Jariwala, K.; Rycroft, C. H.; Bhown, A. S.; Deem, M. W.; Haranczyk, M.; Smit, B. *Nat. Mater.* **2012**, *11*, 633. (b) Wu, D.; Yang, Q.; Zhong, C.; Liu, D.; Huang, H.; Zhang, W.; Maurin, G. *Langmuir* **2012**, *28*, 12094. (c) Gómez-Gualdrón, D. A.; Wilmer, C. E.; Farha, O. K.; Hupp, J. T.; Snurr, R. Q. *J. Phys. Chem. C* **2014**, *118*, 6941. (d) Chung, Y. G.; Camp, J.; Haranczyk, M.; Sikora, B. J.; Bury, W.; Krungleviciute, V.; Yildirim, T.; Farha, O. K.; Sholl, D. S.; Snurr, R. Q. *Chem. Mater.* **2014**, *26*, 6185. (e) Fernandez, M.; Boyd, P. G.; Daff, T. D.; Aghaji, M. Z.; Woo, T. K. *J. Phys. Chem. Lett.* **2014**, *5*, 3056. (f) Simon, C. M.; Mercado, R.; Schnell, S. K.; Smit, B.; Haranczyk, M. *Chem. Mater.* **2015**, *27*, 4459.
(10) Gómez-Gualdrón, D. A.; Gutov, O. V.; Krungleviciute, V.; Borah, B.; Mondloch, J. E.; Hupp, J. T.; Yildirim, T.; Farha, O. K.; Snurr, R. Q. *Chem. Mater.* **2014**, *26*, 5632.
(11) (a) Chowdhury, P.; Bikkina, C.; Meister, D.; Dreisbach, F.; Gumma, S. *Microporous Mesoporous Mater.* **2009**, *117*, 406. (b) Farha, O. K.; Ozgur Yazaydin, A.; Eryazici, I.; Malliakas, C. D.; Hauser, B. G.; Kanatzidis, M. G.; Nguyen, S. T.; Snurr, R. Q.; Hupp, J. T. *Nat. Chem.* **2010**, *2*, 944. (c) Farha, O. K.; Eryazici, I.; Jeong, N. C.; Hauser, B. G.; Wilmer, C. E.; Sarjeant, A. A.; Snurr, R. Q.; Nguyen, S. T.; Yazaydın, A. Ö.; Hupp, J. T. *J. Am. Chem. Soc.* **2012**, *134*, 15016. (d) Grunker, R.; Bon, V.; Muller, P.; Stoeck, U.; Krause, S.; Mueller, U.; Senkovska, I.; Kaskel, S. *Chem. Commun.* **2014**, *50*, 3450.
(12) (a) Kolotilov, S. V.; Pavlishchuk, V. V. *Theor. Exp. Chem.* **2009**, *45*, 75. (b) Goldsmith, J.; Wong-Foy, A. G.; Cafarella, M. J.; Siegel, D. J. *Chem. Mater.* **2013**, *25*, 3373.
(13) Fernandez, M.; Woo, T. K.; Wilmer, C. E.; Snurr, R. Q. *J. Phys. Chem. C* **2013**, *117*, 7681.
(14) (a) Brunauer, S.; Emmett, P. H.; Teller, E. *J. Am. Chem. Soc.* **1938**, *60*, 309. (b) Sing, K. S. W. In *Adsorption by Powders and Porous Solids*, 2nd ed.; Rouquerol, F., Rouquerol, J., Sing, K. S. W., Llewellyn, P., Maurin, G., Eds.; Academic Press: Oxford, 2014; p 237.
(15) Furukawa, H.; Ko, N.; Go, Y. B.; Aratani, N.; Choi, S. B.; Choi, E.; Yazaydin, A. Ö.; Snurr, R. Q.; O'Keeffe, M.; Kim, J.; Yaghi, O. M. *Science* **2010**, *329*, 424.
(16) Wang, T. C.; Bury, W.; Gomez-Gualdron, D. A.; Vermeulen, N. A.; Mondloch, J. E.; Deria, P.; Zhang, K.; Moghadam, P. Z.; Sarjeant, A. A.; Snurr, R. Q.; Stoddart, J. F.; Hupp, J. T.; Farha, O. K. *J. Am. Chem. Soc.* **2015**, *137*, 3585.
(17) (a) Walton, K. S.; Snurr, R. Q. *J. Am. Chem. Soc.* **2007**, *129*, 8552. (b) Bae, Y.-S.; Yazaydın, A. Ö.; Snurr, R. Q. *Langmuir* **2010**, *26*, 5475.
(18) Düren, T.; Millange, F.; Férey, G.; Walton, K. S.; Snurr, R. Q. *J. Phys. Chem. C* **2007**, *111*, 15350.
(19) (a) Rouquerol, J.; Llewellyn, P.; Rouquerol, F. In *Studies in Surface Science and Catalysis*; Llewellyn, P. L., Rodriquez-Reinoso, F., Rouquerol, J., Seaton, N., Eds.; Elsevier: Amsterdam, 2007; Vol. *160*, p 49. (b) Streppel, B.; Hirscher, M. *Phys. Chem. Chem. Phys.* **2011**, *13*, 3220. (c) Ladavos, A. K.; Katsoulidis, A. P.; Iosifidis, A.; Triantafyllidis, K. S.; Pinnavaia, T. J.; Pomonis, P. J. *Microporous Mesoporous Mater.* **2012**, *151*, 126. (d) Hammond, K. D.; Conner, W. C., Jr. In *Advances in Catalysis*; Gates, B. C., Jentoft, F. C., Eds.; Academic Press: Waltham, MA, 2013; Vol. *56*, p 1. (e) Hart, K. E.; Abbott, L. J.; Colina, C. M. *Mol. Simul.* **2013**, *39*, 397. (f) Llewellyn, P.; Maurin, G.; Rouquerol, J. In *Adsorption by Powders and Porous Solids*, 2nd ed.; Rouquerol, F., Rouquerol, J., Sing, K. S. W., Llewellyn, P., Maurin, G., Eds.; Academic Press: Oxford, 2014; p 565. (g) Senkovska, I.; Kaskel, S. *Chem. Commun.* **2014**, *50*, 7089. (h) Thommes, M.; Cychosz, K. *Adsorption* **2014**, *20*, 233. (i) De Lange, M. F.; Vlugt, T. J. H.; Gascon, J.; Kapteijn, F. *Microporous Mesoporous Mater.* **2014**, *200*, 199.
(20) Thommes, M.; Kaneko, K.; Neimark, A. V.; Olivier, J. P.; Rodriguez-Reinoso, F.; Rouquerol, J.; Sing, K. S. W. *Pure Appl. Chem.* **2015**, DOI: 10.1515/pac-2014-1117.
(21) (a) Farha, O. K.; Hupp, J. T. *Acc. Chem. Res.* **2010**, *43*, 1166. (b) Stock, N.; Biswas, S. *Chem. Rev.* **2012**, *112*, 933. (c) Mondloch, J. E.; Karagiaridi, O.; Farha, O. K.; Hupp, J. T. *CrystEngComm* **2013**, *15*, 9258.
(22) (a) Chae, H. K.; Siberio-Perez, D. Y.; Kim, J.; Go, Y.; Eddaoudi, M.; Matzger, A. J.; O'Keeffe, M.; Yaghi, O. M. *Nature* **2004**, *427*, 523. (b) Stoeck, U.; Krause, S.; Bon, V.; Senkovska, I.; Kaskel, S. *Chem. Commun.* **2012**, *48*, 10841.
(23) Potoff, J. J.; Siepmann, J. I. *AIChE J.* **2001**, *47*, 1676.
(24) Rappe, A. K.; Casewit, C. J.; Colwell, K. S.; Goddard, W. A.; Skiff, W. M. *J. Am. Chem. Soc.* **1992**, *114*, 10024.
(25) Dubbeldam, D.; Calero, S.; Ellis, D. E.; Snurr, R. Q. *Mol. Simul.* **2016**, *42*, 81.
(26) Do, D. D.; Herrera, L.; Fan, C.; Wongkoblap, A.; Nicholson, D. *Adsorption* **2010**, *16*, 3.
(27) Cavka, J. H.; Jakobsen, S.; Olsbye, U.; Guillou, N.; Lamberti, C.; Bordiga, S.; Lillerud, K. P. *J. Am. Chem. Soc.* **2008**, *130*, 13850.
(28) Morris, W.; Volosskiy, B.; Demir, S.; Gándara, F.; McGrier, P. L.; Furukawa, H.; Cascio, D.; Stoddart, J. F.; Yaghi, O. M. *Inorg. Chem.* **2012**, *51*, 6443.
(29) Gutov, O. V.; Bury, W.; Gomez-Gualdron, D. A.; Krungleviciute, V.; Fairen-Jimenez, D.; Sarjeant, A. A.; Snurr, R. Q.; Hupp, J. T.; Yildirim, T.; Farha, O. K. *Chem. - Eur. J.* **2014**, *20*, 12389.
(30) Zhao, D.; Yuan, D.; Sun, D.; Zhou, H.-C. *J. Am. Chem. Soc.* **2009**, *131*, 9186.
(31) Yan, Y.; Lin, X.; Yang, S.; Blake, A. J.; Dailly, A.; Champness, N. R.; Hubberstey, P.; Schroder, M. *Chem. Commun.* **2009**, 1025.
(32) Peng, Y.; Srinivas, G.; Wilmer, C. E.; Eryazici, I.; Snurr, R. Q.; Hupp, J. T.; Yildirim, T.; Farha, O. K. *Chem. Commun.* **2013**, *49*, 2992.

DOI: 10.1021/jacs.5b10266
J. Am. Chem. Soc. 2016, 138, 215−224